An Improved Impedance Modeling Method of Grid-Tied Inverters With White-Box Property

Zhijie Zeng, Huafeng Xiao, *Senior Member, IEEE*, Chenhui Niu, Jie Chen, *Member, IEEE*, Ziyi Wang, Xu Wu, and Ming Cheng, *Fellow, IEEE*

***Abstract*—Small-signal modeling of grid-tied inverters (GTIs) is an essential work in stability analysis of GTIs-weak grid coupling system. Different from the previous small-signal modeling methods of GTIs with black-box property, a reduced-order modeling method has been proposed in this article to provide an impedance model with white-box property. First, impedance and admittance are seamlessly incorporated into the modeling method, where concepts of partial admittances, partial impedance, active power admittance, and reactive power admittance are especially introduced. As a result, simplified expressions of impedance model of GTIs have been obtained with physical interpretations of *dq* impedances strengthened. After that, dominated relationships between terms of GTI's impedance matrix and its internal physical parts are explicitly revealed to represent white-box property of the proposed impedance model. Specifically, the influence and effect mechanism of feedforward voltage compensation, current controller, phase lock loop, and power points (I_d, I_q) are emphasized based on the proposed impedance model. Finally, perturbations generated independent with PLL are injected into a hardware in-loop experiment platform, and impedance measurement results are provided to verify the conclusions drawn from the improved modeling method.**

***Index Terms*—Admittance, harmonic resonance, impedance, negative resistance, small-signal.**

I. Introduction

With the increasing adoption scale of power electronics interfaces for renewable energy generations, the traditional power system featured as synchronous machine is evolving as power electronics-based power system. As a consequence, distribution networks behave with more and more obvious characteristics of weak grid [1]–[3]. Grid-tied inverters equipped with multiple-timescale controllers are a kind of classical interface units between distributed renewable energy generations and the grid [4], [5]. The interaction between GTIs and weak grid easily leads to broadband resonance and harmonic stability issues, which deteriorate power quality and even endanger the operation of power system [6], [7].

Analysis methods for harmonic stability of grid-connected system mainly include state-space approaches and impedance-based approaches [8]. The state-space approach requires detailed system parameters, then the small-signal characters can be analyzed based on equations containing interior parameters [9], [10], which is the representative characteristics of white-box model. The state-space approaches are generally adopted for bulk power system with fixed parameters and few generators [11]. Yet, due to the wide time scale dynamics of power electronics converters connected into grid, the system order of state-space model will significantly increase and even lead to dimension disaster [12]. Furthermore, the white-box model is non-convenient to verify by measurement, and physical mechanism of resonance cannot be revealed by state-space based stability analysis.

Impedance-based approaches were earlier developed to analyze the interactions of dc–dc converters for dc cascaded system, in which terminal characteristics of converters depicted by transfer functions are extracted, and thus, the stability analysis is performed in frequency domain by dividing the whole system into source subsystem and load subsystem [13]. As operation parameters of renewable energy generations and modern power networks change frequently, the impedance-based black-box modeling approach tends to be more suitable to analyze the stability of coupling system of GTIs and weak grid [14]. When the impedance is single-input and single-output (SISO) black-box model, it not only eliminates the disadvantages of the white-box model but also has the advantages of the white-box model by oriented reshaping of impedance [15], [16]. Furtherly, considering the accuracy limit of SISO model, multi-input and multi-output (MIMO) impedance modeling approaches have been deeply investigated [17], [18].

Generally speaking, MIMO impedance models of GTIs can be classified into sequence impedance model and *dq* impedance model expressed in different coordinate [19]. Currently, GTIs are usually controlled in the *dq* frame to regulate active and reactive power exchanged with power grid, therefore, the *dq* impedance

Manuscript received June 30, 2021; revised September 13, 2021; accepted October 20, 2021. Date of publication October 27, 2021; date of current version December 31, 2021. This work was supported in part by the Headquarters R&D Project of China Huaneng Group under Grant HNKJ21-HF263 and in part by the Foundation of Jiangsu Key Laboratory of Smart Grid Technology and Equipment. Recommended for publication by Associate Editor M. Ordonez. *(Corresponding author: Huafeng Xiao.)*

Zhijie Zeng is with Fujian Electric Power Research Institute, Fuzhou 350003, China (e-mail: zengzhijief1996@163.com).

Ziyi Wang and Xu Wu are with the School of Electrical Engineering, Southeast University, Nanjing 210096, China (e-mail: 494854942@qq.com; 230208784@seu.edu.cn).

Huafeng Xiao is with the College of Electrical Engineering, Southeast University, Nanjing 210096, China (e-mail: xiaohf@seu.edu.cn).

Chenhui Niu is with China Huaneng Jiangsu Company, Shenyang 110870, China (e-mail: niuchenhui@sgepri.sgcc.com.cn).

Jie Chen is with Electrical Engineering Department, Nanjing University of Aeronautics and Astronautics, Nanjing 210016, China (e-mail: chen_jie@nuaa.edu.cn).

Ming Cheng is with the Department of Electrical Engineering, Southeast University, Nanjing 210096, China (e-mail: mcheng@seu.edu.cn).

Color versions of one or more figures in this article are available at https://doi.org/10.1109/TPEL.2021.3123133.

Digital Object Identifier 10.1109/TPEL.2021.3123133

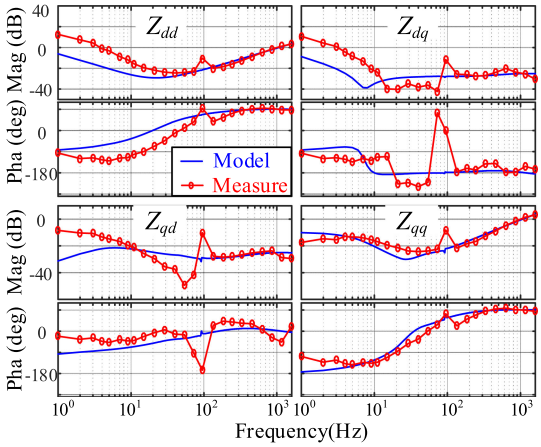

Fig. 1. Impedance curves of GTIs with and without FVC.

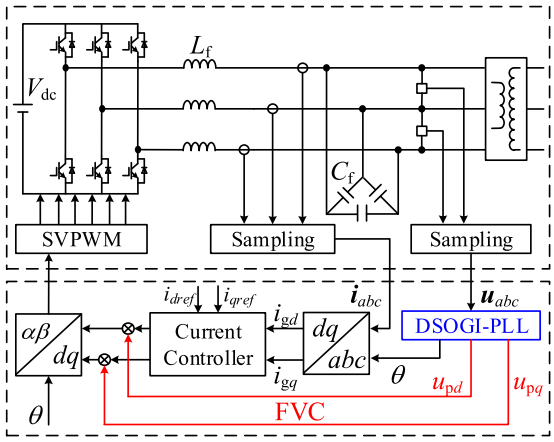

Fig. 2. Grid-tied inverters with feedforward control.

model is easier to build connections with control blocks of GTIs [20]. Based on the small-signal model of dynamic error of phase lock loop (PLL) in [21], Wen *et al.* [22] established a full-order *dq* impedance model for GTIs, and effects of PLL and feedback control on impedance were analyzed by comparing impedance curves. This modeling approach was further developed to discuss influences of grid impedance and filter parameters on the interaction stability of inverters-grid connected system [23]. Because the three-phase inverter is presented as a coupled dual-input and dual-output system in *dq* coordinate, subsequent matrix calculations weakened connections between impedance terms and physical parts of GTIs, and thus, it is difficult to find out the interaction mechanism between GTIs' parameters and coupling system stability [24]. In order to avoid multiplex matrix operations, a simplest *dq* impedance model was proposed by ignoring all impedance coupling terms of impedance matrix in [25], but its application range is limited as it only can be used to analyze the stability under unity power factor condition [26]. A small-signal model of the GTI with divided *d*-channel and *q*-channel was proposed to improve stability analysis without matrix calculation in [24], but the relationships between impedance terms and the physical parts of GTIs had not been revealed yet, which is the weakness of MIMO black-box model.

In order to build the relationships discussed above, a simplified small-signal model with enhanced physical interpretation has been proposed in [27] by reducing matrix calculations and ignoring part of coupling terms in the modeling process. In grid-connected system, the feedforward voltage compensator (FVC) is practically applied to improve the grid-in current quality under conditions of the grid voltage distorted [28]. However, the influence of FVC to small-signal model of GTIs has not been discussed and reported in existing publications yet. As shown in Fig. 1, the impedance model was exported without considering FVC while measurement impedance data were obtained from a real GTI controller with FVC based on hardware in-loop experimental platform. It is obvious that there are significant deviations between existing model and real objective, especially in the amplitude-frequency curves of Z_{dd} and Z_{dq}. The contribution of this article is that impedance modeling approaches for GTIs with FVC are proposed and a set of interior-terminal-connections is revealed based on the built reduced-order MIMO impedance model to represent white-box property.

The rest of this article is organized as follows. According to previous modeling approach investigated in [22], Section II first presents a full-order small-signal model of GTIs as a reference of following discussions. After that, a reduced-order impedance modeling method for GTIs with FVC is proposed, and thus, a simplified impedance model is obtained in Section III. Subsequently, the frequency scanning results in experimental platform are provided in Section IV to verify the proposed model. In Section VI, the influence of interior physical parts on terminal impedance is analyzed. Finally, Section VII concludes this article.

II. Full-Order Small-Signal Model

As a common structure of commercial 500 kW grid-tied inverters shown in Fig. 2, the bridge output is connected to grid by a *LC* filter and a step-up transformer. It is worth noting that the feedback signal for current controller (CC) is the filter inductor current.

An important issue in the connection of power converters to the grid is the synchronization with the voltage at the point of common coupling (PCC). The phase-locked loop based on synchronous reference frame (SRF-PLL) is conventional means. However, the voltage waveform is prone to be polluted and unbalanced as consequence of the effect of nonlinear loads and asymmetrical grid faults, so dual second-order generalized integrator-based PLL (DSOGI-PLL) is commonly applied to commercial GTIs.

As shown in Fig. 3, the grid voltage is filtered by two second-order generalized integrator-based quadrature signal generator (SOGI-QSG) after transferred from *abc* frame to $\alpha\beta$ frame. The in-quadrature output signals of the adaptive filter are modeled by the following transfer functions:

$$D(s) = \frac{\omega_0 s}{s^2 + \omega_0 s + \omega_0^2} \tag{1}$$

$$Q(s) = \frac{\omega_0^2}{s^2 + \omega_0 s + \omega_0^2}. \tag{2}$$

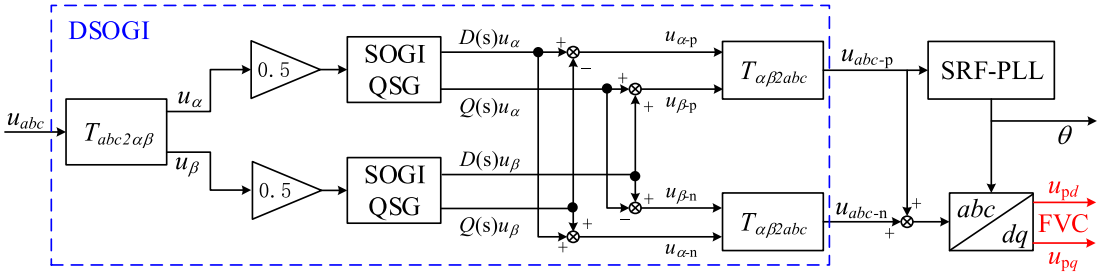

Fig. 3. Scheme of DSOGI-PLL for phase-lock loop and feedforward voltage compensation.

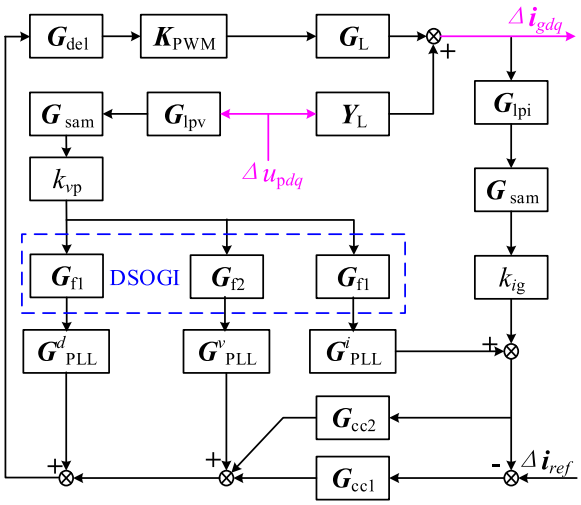

Fig. 4. Accurate small-signal model of grid-tied inverters.

Afterward, the sequence-separated voltage is obtained by calculation, and positive sequence component is applied to generate reference phase in conventional SRF-PLL for coordinate transformation. Meanwhile, it is worth mentioning that feedforward voltage includes both negative sequence and positive sequence as emphasized by red arrows.

The impedance or admittance of the three-phase GTI is basically a breed of small-signal linearization models for nonlinear systems [14]. Based on Figs. 2 and 3, given that $\Delta \boldsymbol{u}_{\mathrm{p}dq}$ denotes the small-signal voltage at PCC, and $\Delta \boldsymbol{i}_{\mathrm{g}dq}$ is the small-signal variable of controlled current in the filter inductor, the small-signal block diagram of GTIs can be described as shown in Fig. 4.

Similar with definitions in [22], $\mathbf{G}_{\mathrm{del}}$ is the transfer function matrix of digital control delay. $\mathbf{G}^{\phi}_{\mathrm{PLL}}$, $\mathbf{G}^{i}_{\mathrm{PLL}}$, and $\mathbf{G}^{v}_{\mathrm{PLL}}$ model small-signal paths from system voltage to duty cycle control signal, current and voltage in controller *dq* frame, respectively. The current PI controller matrix is $\mathbf{G}_{\mathrm{cc1}}$ while the decoupling term in the controller is denoted as $\mathbf{G}_{\mathrm{cc2}}$. Considering that the current controller is based on inductor-current feedback scheme, the inverter-side impedance ($\mathbf{Z}_{\mathrm{i}}$) is modeled similar with *L*-filtered GTI, so $\mathbf{Y}_L$ is the admittance transfer function matrix of filter inductor, and $\mathbf{G}_L$ is equivalent to minus $\mathbf{Y}_L$ due to the inverse definition of current direction.

To model the current sampling branch, $\mathbf{G}_{\mathrm{lp}i}$ represents transfer function matrix of low-pass filter, and $\mathbf{G}_{\mathrm{sam}}$ is introduced due to the half-cycle delay in discrete sampling while k_{ig} is the current sampling coefficient. Symmetrically, $\mathbf{G}_{\mathrm{lpv}}$ is the transfer function matrix of low-pass filter in voltage sampling branch, $k_{\mathrm{p}v}$ is the voltage sampling coefficient while $\boldsymbol{K}_{\mathrm{PWM}}$ is the product of $1/k_{\mathrm{p}v}$ and a second-order identity matrix.

Moreover, two transfer-function matrices $\mathbf{G}_{\mathrm{f1}}$ and $\mathbf{G}_{\mathrm{f2}}$ of equivalent voltage filters are introduced to model the effect of DSOGI-PLL. Since expressions $\mathbf{G}_{\mathrm{f1}}$ and $\mathbf{G}_{\mathrm{f2}}$ in *dq* frame can not be derived directly from transfer functions of $\alpha\beta$ frame, a curve-fitted approach was applied to obtain target transfer functions based on frequency-scan results of DSOGI module. In the small-signal branch of $\mathbf{G}_{\mathrm{f1}}$, the reserved positive sequence voltage in *dq* frame can be described by

$$\begin{cases} \mathbf{G}_{\mathrm{f1}}(1,1) = \mathbf{G}_{\mathrm{f1}}(2,2) = \frac{56\pi}{s+56\pi} - \frac{33s}{s^2+110s+(160\pi)^2} \\ \mathbf{G}_{\mathrm{f1}}(1,2) = -\mathbf{G}_{\mathrm{f1}}(2,1) = \frac{-125.6s}{s^2+100\pi s+(100\pi)^2} \cdot \frac{260\pi}{s+260\pi} \cdot \\ \qquad \cdot \frac{70\pi}{s+70\pi} \end{cases} \tag{3}$$

Likewise, the equivalent filter $\mathbf{G}_{\mathrm{f2}}$ considering both positive sequence and negative sequence can also be derived as shown in the following:

$$\begin{cases} \mathbf{G}_{\mathrm{f2}}(1,1) = \mathbf{G}_{\mathrm{f2}}(2,2) = \frac{56\pi}{s+56\pi} + \frac{110s}{s^2+220s+(200\pi)^2} \\ \mathbf{G}_{\mathrm{f2}}(1,2) = -\mathbf{G}_{\mathrm{f2}}(2,1) = \frac{0.4\cdot(200\pi)^2}{s^2+108\pi s+(200\pi)^2} \cdot \frac{s}{s+200\pi} \cdot \\ \qquad \cdot \frac{s}{s+14\pi} \end{cases} \tag{4}$$

As illustrated in Fig. 5, the characteristic of DSOGI in frequency domain is holistically closed to low-pass filter. Due to that negative sequence component of line frequency is presented as double line frequency, $\mathbf{G}_{\mathrm{f1}}$ and $\mathbf{G}_{\mathrm{f2}}$ differ evidently around 100 Hz. More specifically, $\mathbf{G}_{\mathrm{f1}}$ and $\mathbf{G}_{\mathrm{f2}}$ present as band-stop filter and band-pass filter in the frequency range around double line frequency, respectively.

According to Fig. 3, $\Delta \boldsymbol{u}_{\mathrm{p}dq}$ and $\Delta \boldsymbol{i}_{\mathrm{g}dq}$ are featured as excitation and response to each other. When voltage is interpreted as excitation and current is response, the inverter admittance can be obtained as (5). Alternatively, the full-order impedance of GTIs was derived as inverse matrix of admittance [22]

$$\begin{aligned} \mathbf{Y} = {} & (\mathbf{E}_2 - \mathbf{G}_L\mathbf{K}_{\mathrm{PWM}}\mathbf{G}_{\mathrm{del}} \cdot (\mathbf{G}_{\mathrm{cc2}} - \mathbf{G}_{\mathrm{cc1}})k_{ig}\mathbf{G}_{\mathrm{sam}}\mathbf{G}_{\mathrm{lp}i})^{-1} \\ & \cdot (\mathbf{Y}_L + \mathbf{G}_L\mathbf{K}_{\mathrm{PWM}}\mathbf{G}_{\mathrm{del}}(\mathbf{G}^d_{\mathrm{PLL}}\mathbf{G}_{\mathrm{f1}} + \mathbf{G}^v_{\mathrm{PLL}}\mathbf{G}_{\mathrm{f2}} \\ & + (\mathbf{G}_{\mathrm{cc2}} - \mathbf{G}_{\mathrm{cc1}})\mathbf{G}^i_{\mathrm{PLL}}\mathbf{G}_{\mathrm{f1}})k_{vp}\mathbf{G}_{\mathrm{sam}}\mathbf{G}_{\mathrm{lp}v}). \end{aligned} \tag{5}$$

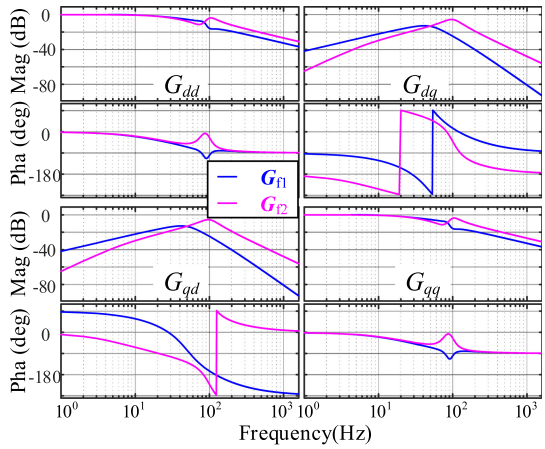

Fig. 5. Bode curves of equivalent filter.

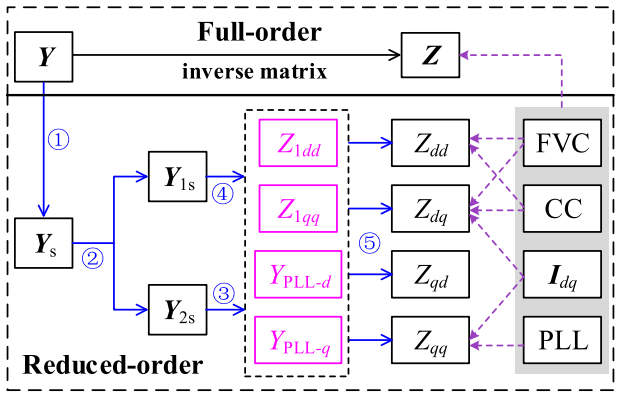

Fig. 6. Comparison of full and reduced order modeling.

It is revealed that the establishment of the full-order impedance model requires lots of matrix operations including coupling terms and matrix inversion, which leads to fuzzy connection between the impedance terms and actual physical segments. In order to eliminate this deficiency, a method for establishing a reduced-order model will be discussed in the following sections.

III. Reduced-Order Small-Signal Modeling

Due to the existence of coupling terms in transfer function matrix, the full-order expressions of impedance terms are complex after lots of matrix multiplication and inverse operations as shown in (5), which further fuzzes the connections between external characteristics and internal parameters. Consequently, reducing matrix operations and simplifying coupling terms are interpreted as the guideline of proposed modeling method, and then two assumptions are introduced as following.

Assumption 1: Considering certain effect frequency-bands of different physical segments, the number of matrices involved in the calculation can be reduced in the case of focusing on certain frequency-band. Specifically, it is divided to low-frequency band (0–20 Hz), medium-frequency band (20–200 Hz) and high frequency band (200–1600 Hz), where 1600 Hz is half of switching frequency of discussed 500 kW inverters.

Assumption 2: Considering that dominant elements in most matrices lie in main-diagonal. If amplitude difference of impedance between the main-diagonal and subdiagonal elements approaches or exceeds 20 dB, the influence of the subdiagonal elements can be ignored.

The order-reduction of low-frequency is first performed. In order to distinguish the modeling processes of full-order model and proposed reduced-order model, a schematic diagram is plotted as shown in Fig. 6, where five steps are introduced to derive individual expressions of elements in the impedance matrix, and thus, explicit connections can be presented by reduced-order impedance model.

As the application of assumption 1 and the first step of reduced-order modeling, matrices are classified into dominant matrices and nondominant matrices during low-frequency band, then the following simplified-admittance is obtained by removing nondominant matrices:

$$\begin{aligned}\mathbf{Y}_{\rm s} = &(\mathbf{E}_2 - \mathbf{G}_L\mathbf{K}_{\rm PWM}(\mathbf{G}_{\rm cc2} - \mathbf{G}_{\rm cc1})k_{ig})^{-1} \\ &\cdot (\mathbf{Y}_L + \mathbf{G}_L(\mathbf{G}^d_{\rm PLL} + \mathbf{G}^v_{\rm PLL} \\ &+ (\mathbf{G}_{\rm cc2} - \mathbf{G}_{\rm cc1})\mathbf{G}^i_{\rm PLL})\mathbf{G}_{\rm sogi}). \end{aligned} \tag{6}$$

Noted that $\mathbf{G}_{\rm sogi}$ is substituted expression of $\mathbf{G}_{\rm f1}$ and $\mathbf{G}_{\rm f2}$, where subdiagonal terms are ignored and the consistent diagonal term ($g_{\rm sogi}$) is simplified to a low-pass filter with a certain cutoff frequency (i.e., 28 Hz).

Second, partial admittances are defined according to the disintegration of simplified admittance in (6). The first partial admittance nonrelevant with PLL and another partial admittance relevant with PLL is shown in (7) and (8), respectively. Referring to assumption 2, decoupling terms in the controller is negligible compared with PI controller ($tf_{\rm cc}$), and thus, $\mathbf{G}_{\rm cc2}$ is removed from expressions of partial admittances

$$\mathbf{Y}_{\rm 1s} = (\mathbf{E}_2 - \mathbf{Y}_L\mathbf{K}_{\rm PWM}\mathbf{G}_{\rm cc1}k_{ig})^{-1} \cdot \mathbf{Y}_L \tag{7}$$

$$\begin{aligned}\mathbf{Y}_{\rm 2s} = &-(\mathbf{E}_2 - \mathbf{Y}_L\mathbf{K}_{\rm PWM}\mathbf{G}_{\rm cc1}k_{ig})^{-1} \\ &\cdot \mathbf{Y}_L \cdot (\mathbf{G}^d_{\rm PLL} + \mathbf{G}^v_{\rm PLL} - \mathbf{G}_{\rm cc1}\mathbf{G}^i_{\rm PLL})\mathbf{G}_{\rm sogi}. \end{aligned} \tag{8}$$

In order to derive individual expressions of partial admittances, related matrices are listed in the following, where $\boldsymbol{I}_{dq}$ is the fundamental grid-in current's amplitude in the given power level, $\boldsymbol{V}_{{\rm c}dq}$ is the fundamental component's amplitude of modulation signal in SVPWM, $\boldsymbol{V}_{{\rm p}d}$ is the fundamental voltage amplitude of PCC. Note that the small-signal models of PLL in (10)–(12) are simplified after focusing on low-frequency band, which is derived from original definition of the literature [22]

$$\mathbf{G}_{\rm cc1} = \begin{bmatrix} -tf_{\rm cc} & 0 \\ 0 & -tf_{\rm cc} \end{bmatrix} \tag{9}$$

$$\mathbf{G}^v_{\rm PLL} = \begin{bmatrix} 1 & 0 \\ 0 & 0 \end{bmatrix} \tag{10}$$

$$\mathbf{G}^d_{\rm PLL} = \begin{bmatrix} 0 & \frac{-V_{cq}}{V_{pd}} \\ 0 & \frac{V_{cd}}{V_{pd}} \end{bmatrix} \tag{11}$$

$$\mathbf{G}_{\mathrm{PLL}}^{i}=\begin{bmatrix}0 & \frac{I_q\cdot k_{ig}}{V_{\mathrm{pd}}\cdot k_{vp}}\\ 0 & \frac{-I_d\cdot k_{ig}}{V_{\mathrm{pd}}\cdot k_{vp}}\end{bmatrix}. \tag{12}$$

As third step, the individual expressions of elements in $\mathbf{Y}_{2\mathrm{s}}$ [referring to (13)] can be derived through the manipulation on (8)–(12)

$$\mathbf{Y}_{2s}=\begin{bmatrix}Y_{2dd} & Y_{\mathrm{PLL}-d}\\ 0 & Y_{\mathrm{PLL}-q}\end{bmatrix}. \tag{13}$$

More specifically, d-channel admittance and q-channel admittance introduced by PLL can be described by (14) and (15), where dominant variables are power points (I_d and I_q) as listed in the end of brackets. It is indicated that there is a positive correlation between the amplitude of $Y_{\mathrm{PLL}\text{-}d}$ and the current value of reactive power. Likewise, there exists a positive correlation between the amplitude of $Y_{\mathrm{PLL}\text{-}q}$ and the current value of active power. Accordingly, $Y_{\mathrm{PLL}\text{-}d}$ and $Y_{\mathrm{PLL}\text{-}q}$ can be defined as reactive power admittance and active power admittance, respectively

$$Y_{\mathrm{PLL}-d}=\left(\frac{V_{\mathrm{cq}}}{V_{\mathrm{pd}}}\cdot\frac{k_{vp}}{k_{ig}tf_{\mathrm{cc}}}-\frac{I_q}{V_{\mathrm{pd}}}\right)\cdot g_{\mathrm{sogi}} \tag{14}$$

$$Y_{\mathrm{PLL}-q}=\left(\frac{V_{\mathrm{cd}}}{V_{\mathrm{pd}}}\cdot\frac{k_{vp}}{k_{ig}tf_{\mathrm{cc}}}+\frac{k_{vp}}{k_{ig}tf_{\mathrm{cc}}}+\frac{I_d}{V_{\mathrm{pd}}}\right)\cdot g_{\mathrm{sogi}}. \tag{15}$$

Considering that I_d is a negative value in normal grid-connected mode, a further look into (15) reveals that phase of active power admittance will be shaped as 180° during low frequency range. The so-called negative resistor behavior of $Y_{\mathrm{PLL}\text{-}q}$ will inspire destabilizing effect when dynamically interacting with the impedance of weak-gird [27].

Notice that subdiagonal terms of $\mathbf{Y}_{1\mathrm{s}}$ are originated from coupling terms of the admittance matrix of filter inductor. Referring to assumption 2, subdiagonal terms of $\mathbf{Y}_{1\mathrm{s}}$ are ignored in the fourth step. Meanwhile, $Y_{2\,dd}$ can be integrated with $Y_{1\,dd}$, which is shown in manipulation of the following:

$$\begin{aligned}\Delta\mathbf{i}_{gdq}&=\begin{bmatrix}Y_{1dd} & Y_{1dq}\\ Y_{1qd} & Y_{1qq}\end{bmatrix}\Delta\mathbf{u}_{pdq}+\begin{bmatrix}Y_{2dd} & Y_{\mathrm{PLL}-d}\\ 0 & Y_{\mathrm{PLL}-q}\end{bmatrix}\Delta\mathbf{u}_{pdq}\\&\approx\begin{bmatrix}Y_{1dd}+Y_{2dd} & 0\\ 0 & Y_{1qq}\end{bmatrix}\Delta\mathbf{u}_{pdq}+\begin{bmatrix}0 & Y_{\mathrm{PLL}-d}\\ 0 & Y_{\mathrm{PLL}-q}\end{bmatrix}\Delta\mathbf{u}_{pdq}.\end{aligned} \tag{16}$$

Subsequently, partial impedances ($Z_{1\,dd}$ and $Z_{1\,qq}$) derived from partial admittances are defined and described by following equations as the result of step 4:

$$Z_{1dd}=\frac{1}{Y_{1dd}+Y_{2dd}}\approx\frac{k_{\mathrm{PWM}}tf_{cc}k_{ig}}{1-g_{\mathrm{sogi}}} \tag{17}$$

$$Z_{1qq}=\frac{1}{Y_{1qq}}\approx k_{\mathrm{PWM}}tf_{cc}k_{ig}. \tag{18}$$

In the final step, an equivalent equation of (19) is derived as follows, where partial impedances, active-power admittance, and reactive-power admittance are synthesized to model the connection between small-signal voltages and currents:

$$\begin{bmatrix}1 & Z_{1dd}Y_{\mathrm{PLL}-d}\\ 0 & 1+Z_{1qq}Y_{\mathrm{PLL}-q}\end{bmatrix}\begin{bmatrix}\Delta u_{\mathrm{pd}}\\ \Delta u_{\mathrm{pq}}\end{bmatrix}=\begin{bmatrix}Z_{1dd} & 0\\ 0 & Z_{1qq}\end{bmatrix}\begin{bmatrix}\Delta i_{gd}\\ \Delta i_{gq}\end{bmatrix}. \tag{19}$$

As shown in the following, the impedance expression with reduced-order was obtained after further manipulation of (19), which is the result of order-reduction in low-frequency band:

$$\mathbf{Z}\approx\begin{bmatrix}Z_{1dd} & \frac{-Z_{1dd}Z_{1qq}Y_{\mathrm{PLL}-d}}{1+Z_{1qq}Y_{\mathrm{PLL}-q}}\\ 0 & \frac{Z_{1qq}}{1+Z_{1qq}Y_{\mathrm{PLL}-q}}\end{bmatrix}. \tag{20}$$

In the order-reduction of high-frequency band, considering that the influence of PLL dynamic error on the small-signal modeling of GTIs disappears, the admittance and impedance expressions can be simplified to the following according to assumption 1:

$$\mathbf{Y}=(\mathbf{E}_2+\mathbf{Y}_Lk_{\mathrm{PWM}}\mathbf{G}_{\mathrm{del}}(\mathbf{G}_{\mathrm{cc2}}-\mathbf{G}_{\mathrm{cc1}})k_{ig}\mathbf{G}_{\mathrm{sam}})^{-1}\cdot\mathbf{Y}_L \tag{21}$$

$$\mathbf{Z}=\mathbf{Z}_L+k_{\mathrm{PWM}}k_{ig}\mathbf{G}_{\mathrm{del}}\mathbf{G}_{\mathrm{sam}}(\mathbf{G}_{\mathrm{cc2}}-\mathbf{G}_{\mathrm{cc1}})). \tag{22}$$

Furthermore, the application of assumption 2 brings out a more concise result without coupling terms as shown in the following:

$$\mathbf{Z}\approx\mathbf{E}_2\cdot\left(Z_L+\frac{k_{ig}}{k_{vp}}k_{\mathrm{pcc}}g_{\mathrm{del}}g_{\mathrm{sam}}\right). \tag{23}$$

In addition to medium-frequency band, reduced-order admittance is obtained as (24) referring to assumption 1, and reduced-order impedance is the inverse of admittance matrix. Since the subdiagonal terms of matrices in (24) are nonignorable, the order-reduction based on assumption 2 is not performed in in medium-frequency band

$$\begin{aligned}\mathbf{Y}=&(\mathbf{E}_2-\mathbf{G}_Lk_{\mathrm{PWM}}k_{ig}(\mathbf{G}_{\mathrm{cc2}}-\mathbf{G}_{\mathrm{cc1}}))^{-1}\\&\cdot(\mathbf{Y}_L+\mathbf{G}_L(\mathbf{G}_{\mathrm{PLL}}^{d}\mathbf{G}_{\mathrm{f1}}+\mathbf{G}_{\mathrm{PLL}}^{v}\mathbf{G}_{\mathrm{f2}}\\&+(\mathbf{G}_{\mathrm{cc2}}-\mathbf{G}_{\mathrm{cc1}})\mathbf{G}_{\mathrm{PLL}}^{i}\mathbf{G}_{\mathrm{f1}})).\end{aligned} \tag{24}$$

As revealed by the integration of (14), (15), (17), (18), (20), and (23), individual expressions of elements in the impedance matrix are obtained, which provides the bedrock of white-box property analysis. Although the derivation and discussion above are performed based on a certain current-controlled GTI, it is worth noting that the principle of simplifying coupling terms and reducing matrix operation can also be applied to the modeling of GTIs with different control scheme.

IV. Model Verification

In order to verify the small-signal model of GTIs with FVC established in previous sections, a real-time digital simulation (RTDS)-based hardware in-loop experimental platform was built as shown in Fig. 7. More specifically, hardware structure of the experiment platform is shown in Fig. 8. The model of power-stage was established in the commercial software (RSCAD) of the upper host-computer connected with RTDS racks. It is worth noting that the controllers were practically applied in

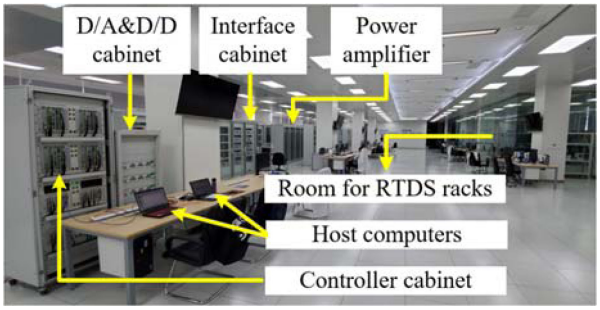

Fig. 7. Hardware in-loop experimental platform.

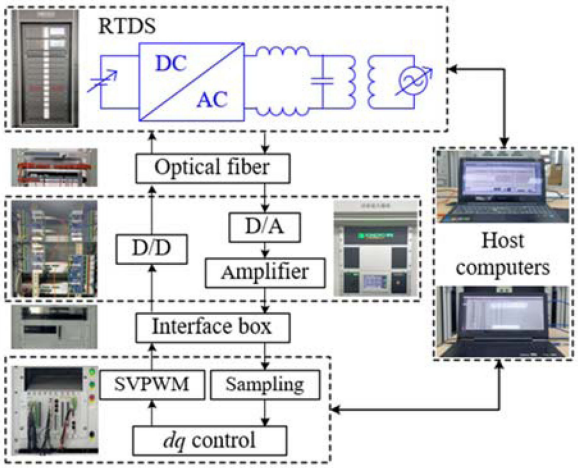

Fig. 8. Hardware structure of the experimental platform.

TABLE I
PARAMETERS OF 500 KW GTIS

Symbol	Description	Value
V_{dc}	Input dc voltage	700V
V_{g0}	Line voltage of transformer in primary-side	315V
V_{g1}	Line voltage of secondary-side	10kV
i_{dref}	D channel current reference	-800A
i_{qref}	Q channel current reference	0/-600A
ω	Line frequency	2π*50rad/s
L	Inductance of inverter output inductor	150uH
C_f	Capacitance of filter capacitor	80uF
R_L	Resistance of inverter inductor self-resistor	20mΩ
f_{sw}	Switching frequency	3.2kHz
k_{pcc}	Proportional gain of current controller	0.125
k_{icc}	Integrator gain of current control	16
T_{del}	Time delay due to digital control and PWM	$1.5/f_{sw}$
k_{pPLL}	Proportional gain of current controller	0.25
k_{iPLL}	Integrator gain of current control	4
k_{pv}	Voltage sampling coefficient for control	23
k_{ig}	Current sampling coefficient for control	6.3

photovoltaic generation system, so current signals and voltage signals are transferred by D/A and amplifier to match the input requirements of the controller's built-in sampling board. As the output signals of controller box, the driving timing generated by SVPWM is sent to RTDS racks after amplitude modulation of D/D, and all of control signals are monitored by the underlying host-computer. Moreover, it should be noted that parameters of 500 kW GTIs are shown in Table I, which are also parameters for analysis in Section V.

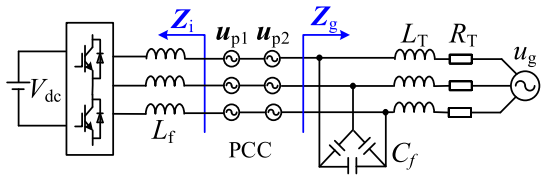

Fig. 9. Circuit for impedance measurement.

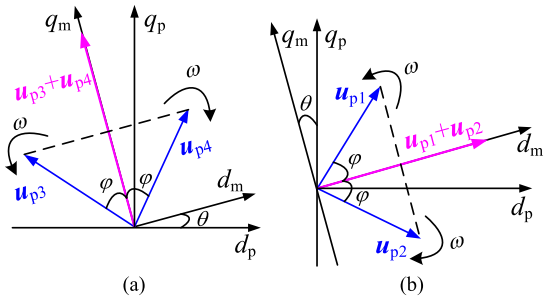

Fig. 10. Composing of perturbation-voltage vector. (a) *d*-axis. (b) *q*-axis.

As shown in Fig. 9, the voltage-based injection approach is used, in which three-phase perturbation voltages are injected at PCC to excite small-signal current disturbance. Subsequently, the target data were obtained with voltage and current collected in a series of interested frequencies. After all quantities are transformed into *dq* frame, the small-signal *dq* impedance characterizes the relationship between small variations of *dq* voltages and *dq* currents in frequency domain, which is expressed by matrix as shown in the following:

$$\begin{bmatrix}\Delta u_d(\omega)\\ \Delta u_q(\omega)\end{bmatrix}=\begin{bmatrix}Z_{idd}(\omega) & Z_{idq}(\omega)\\ Z_{iqd}(\omega) & Z_{iqq}(\omega)\end{bmatrix}\begin{bmatrix}\Delta i_d(\omega)\\ \Delta i_q(\omega)\end{bmatrix}. \tag{25}$$

Since the impedance matrix consists of four unknowns, two linearly independent sets of perturbations are needed in the impedance measurement. Previous research has shown that small-signal perturbations generated dependent on the result of PLL are prone to nonignorable deterioration of measurement accuracy [29]. To avoid this issue, a perturbations-generated approach independent with PLL is adopted in this article.

Considering that three-phase voltages in *abc* frame are presented as rotating vectors in *dq* frame, a set of quadrated perturbation-voltage vector with the nonrotated characteristic can be composed as shown in Fig. 10. Noted that virtual synchronous rotation frame in measurement system is introduced as d_m and q_m while another frame synchronous with PCC voltage is denoted by d_p and q_p. Once the vectors with the same rotation speed are symmetrical to the d_m, the resultant vectors are obtained as *d*-axis voltage disturbances in the view of measurement *dq* frame. Furthermore, the *q*-axis voltage disturbances are composed by changing the phases of perturbation-voltage with frequency and amplitude remained. Though non-synchronization exists between measurement *dq* frame and PCC-voltage-based *dq* frame, two composed perturbation vectors are still linearly independent in the view of PCC-voltage-based *dq* frame, which proves that the result of PLL is non-indispensable in the generation process of perturbation signals.

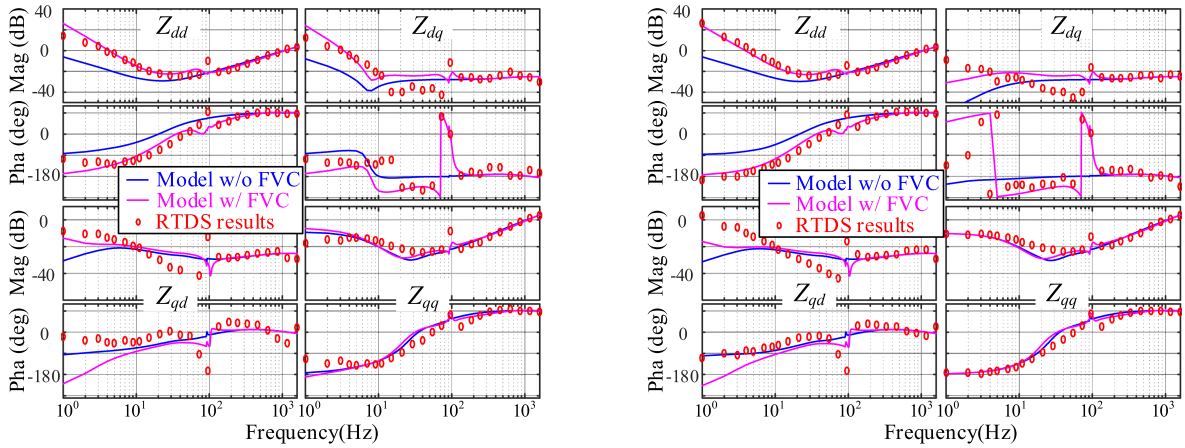

Fig. 11. Measurement results compared with theoretical model. (a) Nonunity power factor case (PF = 0.8). (b) Unity power factor case.

TABLE II
CONNECTIONS BETWEEN GTI'S IMPEDANCE AND PHYSICAL PARTS

Impedance	Low-frequency band	High-frequency band
Z_{dd}	CC、FVC	Filter、k_{pcc}、digital control
Z_{dq}	CC、FVC、I_d 、I_q	Negligible
Z_{qd}	Negligible	Negligible
Z_{qq}	CC、I_d、PLL	Filter、k_{pcc}、digital control

After synthesizing the corresponding data of theorical models and RTDS-based frequency scanning results, the bode plots of GTIs' impedance in cases of different power points are shown in Fig. 11. It can be noticed that theoretical models with FVC and without FVC are over-plotted to simultaneously compare with RTDS-based laboratory measurement results. Referring to the matching effect of two models and final measurement results, large discrepancy between the first group impedance curves and measurement results verifies the necessity of FVC modeling. On the contrary, the impedance date extracted from RTDS-based experiment is well consistent with the second group impedance curves with exception of Z_{dq} and Z_{qd} during low-frequency range. The latter discrepancy results from the sensitivity to small measurement error in the case that both the real part and the imaginary part of GTI impedance are close to zero.

V. INTERIOR-TERMINAL CONNECTION ANALYSIS

It is well known that *dq* impedance is a type of black-box MIMO model after linearization in synchronous coordinate. In order to provide impedance model with white-box property, the proposed reduced-order model is applied to reveal the influence of interiors and their mechanism. More specifically, connections between terms of GTI's impedance matrix and its physical parts are clearly revealed, where FVC, CC, PLL, filter, digital control (sampling delay, calculation delay), and power points (I_d, I_q) are emphasized as shown in Table II. As transition band between low-frequency and high-frequency, vague connections around medium-frequency band were not included in the table followed.

According to derived expression in (17), the impedance curves of Z_{dd} are mainly shaped by PWM coefficient, current sampling coefficient, CC and equivalent filter of SOGI introduced by FVC. It is outstandingly displayed by Fig. 1 that VFC leads to drastic change in the bode curves of Z_{dd}, which can be explained by the proposed simplified model as comparison performed in the following.

In the case of GTI controlled without FVC, $Y_{2\,dd}$ of (13) is replaced by zero due to the disappearance of Gv PLL [referring to (11)] in matrix operation. After that, equations of $Z_{1\,dd}$ and $Z_{1\,qq}$ can be rewritten as follows:

$$Z_{1dd} = Z_{1qq} \approx k_{\text{PWM}} t f_{cc} k_{ig}. \tag{26}$$

By comparison of (17) and (26), the denominator of $Z_{1\,dd}$ is redefined to (1-g_{sogi}) due to existence of VFC, which is also the denominator of Z_{dd}. Since that the denominator of impedance equation is approximately redefined from one to zero in the frequency range under cutoff frequency of g_{sogi}, outstanding improvement of Z_{dd}'s amplitude-frequency curve is inevitable. Simultaneously, the positive phase-frequency characteristic of (1-g_{sogi}) introduces decreasing of Z_{dd}'s phase-frequency curve.

Likewise, assuming that interesting frequency band is still focused onto low-frequency range, individual expression of Z_{dq} is obtained as

$$Z_{dq} \approx \frac{k_{\text{PWM}} t f_{cc} k_{ig}}{1 - g_{\text{sogi}}} \cdot \frac{I_q}{I_d} \tag{27}$$

which indicated that there is close relation between Z_{dd} and Z_{dq}. As consequence of FVC, the higher amplitude of Z_{dd} also brings out the improvement of Z_{dq}. Additionally, power points play an important role in the curve-shaping of Z_{dq}. If GTIs operates in unity-power-factor case, the amplitude of Z_{dq} is negligible compared with Z_{dd}. On the contrary, the nonnegligible amplitude of Z_{dq} will be increased with an improved reactive-power-current value.

As the further derivation of (20), a simplified expression of Z_{qq} is obtained as shown in (28), which reveals that Z_{qq} is mainly determined by power points, CC and g_{sogi} introduced by PLL. More specifically, its amplitude has a negative interrelation to

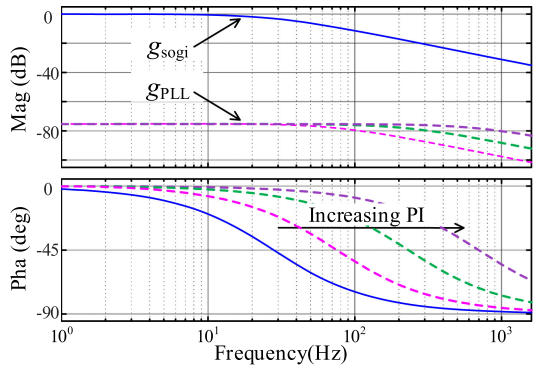

Fig. 12. Comparison of g_{sogi} and g_{PLL} with different PLL parameters.

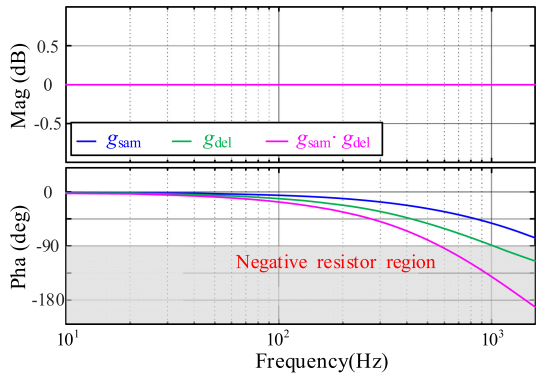

Fig. 13. Bode curves of g_{sam} and g_{del}.

the value of active-power-current but independent to reactive-power-current. It is worthwhile to point out that I_d is negative during inverter operation mode, but positive in rectifier operation mode, so negative resistor behavior is only found in inverter operation mode

$$Z_{qq} \approx \frac{V_{\mathrm{pd}} k_{ig} t f_{\mathrm{cc}}}{(V_{cd} k_{vp} + I_d k_{ig} t f_{\mathrm{cc}} + k_{vp} V_{\mathrm{pd}}) \cdot g_{\mathrm{sogi}}}. \tag{28}$$

The investigations of previous pieces of literature show that the frequency range of negative resistor in Z_{qq} was determined by g_{PLL} as shown in (29), where tf_{PLL} is the PI controller of PLL [21]–[23]. To provide the bedrock for performing analysis of negative resistor behavior, bode curves of g_{sogi} and g_{PLL} are plotted in Fig. 12. It can be noticed that features of low-pass filter are presented with different cutoff frequencies in those curves, where larger PLL parameter cases correspond to the larger cutoff frequency. A further look into the bode plots reveals that the cutoff frequency of g_{sogi} is the smallest compared with all groups of g_{PLL}, and thus, the frequency range of negative resistor is finally determined by g_{sogi}. As a new conclusion drawn from reduced-order model, PLL parameters may not affect the frequency range of negative resistance behavior in the case that PLL is applied with SOGI filter to realize sequence separation

$$g_{\mathrm{PLL}} = \frac{t f_{\mathrm{PLL}}}{s + V_{\mathrm{pd}} \cdot k_{vp} \cdot t f_{\mathrm{PLL}}}. \tag{29}$$

In the impedance analysis of high-frequency band, symmetrical impedance curves are shaped by the L filter and digital control referring to (22) and (23). The bode curves of g_{del} and g_{sam} introduced by digital control are shown in Fig. 13, the amplitude–frequency characteristics will not affect inverter impedance while the phase-shift effect can significantly shape the impedance in high-frequency band. Since they are connected in series with the CC, the proportional coefficient of CC (k_{pcc}) provides a positive resistor component for the inverter impedance in low-frequency band. However, in high-frequency band, k_{pcc} will produce negative resistor component under the effect of digital control, which deteriorates the stability of inverter-grid connected system.

For example, impedance of GTI with different power points, different CC parameters and different PLL parameters are plotted in Figs. 14–16, respectively. The drastic variation of Z_{dd}

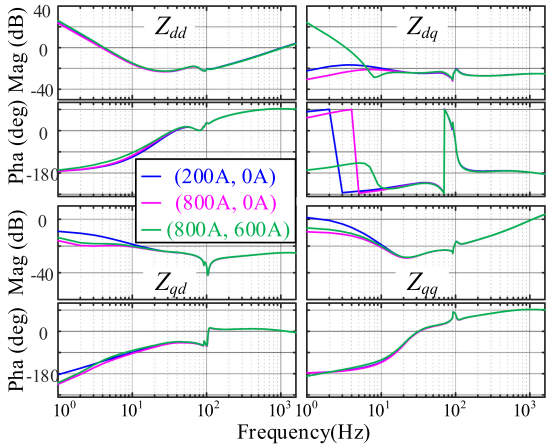

Fig. 14. Impedance of GTI with different power points.

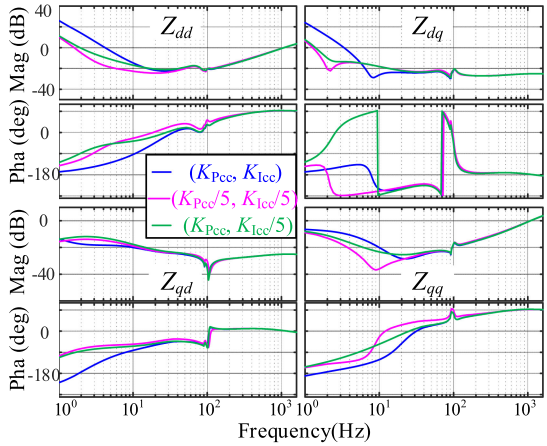

Fig. 15. Impedance of GTI with different CC parameters.

curves only happens in case that CC parameters are changed, which matches the conclusion drawn from (20). Curves of Z_{dq} are reshaped when power points and CC parameters are changed, but nonreshaped with varying PLL parameters, which is in consistent with the conclusion drawn from (27). As expected results associated with (28), the amplitudes of Z_{qq} are decreased with the increasing active-power currents, and bandwidth of negative resistor behavior was not lengthened or shortened by changed PLL parameters.

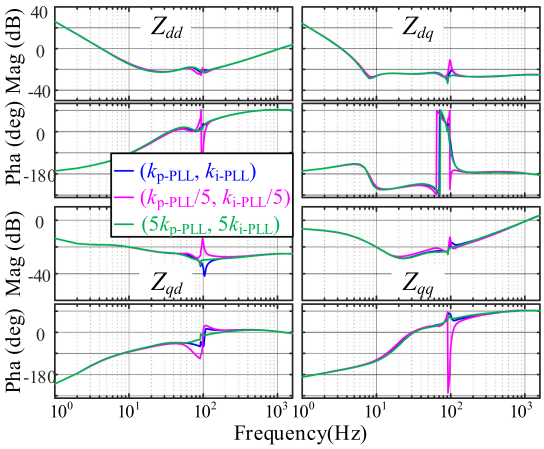

Fig. 16. Impedance of GTI with different PLL parameters.

In addition to Z_{qd}, it is ignorable referring to the simplified impedance expression. Furthermore, impedance curves of Z_{qd} in Figs. 14–16 reveal that its amplitudes are lowest and nearly independent with power points, CC and PLL, which supports the negligibility derived from theorical analysis.

Based on black-box model, the influence of control loops on impedance is analyzed qualitatively by comparing the impedance curves with different parameters [22]. Differently, the influence is quantitatively revealed by derived formulas of reduced-order model, and thus, the provided white-box property advantages the design-oriented analysis and reshaping of inverter impedance.

VI. Conclusion

A full-order *dq* impedance model of GTIs controlled with FVC and DSOGI-PLL has been first established and verified by experimental measurement in this article. Furthermore, a reduced-order small-signal impedance modeling method for GTIs was proposed, where individual expressions of elements in the impedance matrix was derived by reducing matrix operations and simplified coupling terms after focusing on certain frequency band. Specially, it is found that the impact of feedforward voltage lies in impedances Z_{dd} and Z_{dq} featured as increased amplitude and decreased phase. In the research about PLL and CC, the increase of PLL bandwidth has no influence on negative resistor characteristic due to the existence of sequence-separation, but CC introduces negative resistor component in high-frequency band under the effect of digital control. Finally, the improved impedance model with white-box property has been provided for further research about oriented reshaping of MIMO impedance and stability improvement of inverter-grid connected system.

References

[1] M. Lu, X. Wang, P. C. Loh, and F. Blaabjerg, "Resonance interaction of multiparallel grid-connected inverters with LCL filter," *IEEE Trans. Power Electron.*, vol. 32, no. 2, pp. 894–899, Feb. 2017.

[2] R. Luhtala, T. Messo, T. Reinikka, J. Sihvo, T. Roinila, and M. Vilkko, "Adaptive control of grid-connected inverters based on real-time measurements of grid impedance: DQ-domain approach," in *Proc. IEEE Energy Convers. Congr. Expo.*, 2017, pp. 69–75.

[3] K. Song, M. Wu, and S. Yang, "High-order harmonic resonances in traction power supplies: A review based on railway operational data, measurements and experience," *IEEE Trans. Power Electron.*, vol. 35, no. 99, pp. 2501–2518, Mar. 2019.

[4] X. Zhang, D. Xia, Z. Fu, G. Wang, and D. Xu, "An improved feedforward control method considering PLL dynamics to improve weak grid stability of grid-connected inverters," *IEEE Trans. Ind. Appl.*, vol. 54, no. 5, pp. 5143–5151, Sep./Oct. 2018.

[5] X. Wang, L. Harnefors, and F. Blaabjerg, "Unified impedance model of grid-connected voltage-source converters," *IEEE Trans. Power Electron.*, vol. 33, no. 2, pp. 1775–1787, Feb. 2018.

[6] R. N. Beres, X. Wang, M. Liserre, F. Blaabjerg, and C. L. Bak, "A review of passive power filters for three-phase grid-connected voltage-source converters," *IEEE J. Emerg. Sel. Topics Power Electron.*, vol. 4, no. 1, pp. 54–69, Jan. 2016.

[7] J. Sun, G. Wang, X. Du, and H. Wang, "A theory for harmonics created by resonance in converter-grid systems," *IEEE Trans. Power Electron.*, vol. 34, no. 4, pp. 3025–3029, Apr. 2019.

[8] X. Wang and F. Blaabjerg, "Harmonic stability in power electronic-based power systems: Concept, modeling, and analysis," *IEEE Trans. Smart Grid*, vol. 10, no. 3, pp. 2858–2870, May 2019.

[9] Y. Wang, X. Wang, F. Blaabjerg, and Z. Chen, "Harmonic instability assessment using state-space modeling and participation analysis in inverter-fed power systems," *IEEE Trans. Ind. Electron.*, vol. 64, no. 1, pp. 806–816, Jan. 2017.

[10] M. Cespedes and J. Sun, "Impedance modeling and analysis of grid-connected voltage-source converters," *IEEE Trans. Power Electron.*, vol. 29, no. 3, pp. 1254–1261, Mar. 2014.

[11] W. Cao, Y. Ma, L. Yang, F. Wang, and L. M. Tolbert, "D–Q impedance based stability analysis and parameter design of three-phase inverter-based AC power systems," *IEEE Trans. Ind. Electron.*, vol. 64, no. 7, pp. 6017–6028, Jul. 2017.

[12] H. Liu, X. Xie, and W. Liu, "An oscillatory stability criterion based on the unified impedance network model for power systems with high-penetration renewables," *IEEE Trans. Power Syst.*, vol. 33, no. 3, pp. 3472–3485, May 2018.

[13] F. Xiao gang, L. Jinjun, and F. C. Lee, "Impedance specifications for stable DC distributed power systems," *IEEE Trans. Power Electron.*, vol. 17, no. 2, pp. 157–162, Mar. 2002.

[14] J. Sun, "Small-signal methods for AC distributed power systems–A review," *IEEE Trans. Power Electron.*, vol. 24, no. 11, pp. 2545–2554, Nov. 2009.

[15] L. Harnefors, X. Wang, A. G. Yepes, and F. Blaabjerg, "Passivity-based stability assessment of grid-connected VSCs—An overview," *IEEE J. Emerg. Sel. Topics Power Electron.*, vol. 4, no. 1, pp. 116–125, Jan. 2016.

[16] D. Yang, X. Ruan, and H. Wu, "Impedance shaping of the grid-connected inverter with LCL filter to improve its adaptability to the weak grid condition," *IEEE Trans. Power Electron.*, vol. 29, no. 11, pp. 5795–5805, Nov. 2014.

[17] T. Roinila, T. Messo, and E. Santi, "MIMO-identification techniques for rapid impedance-based stability assessment of three-phase systems in DQ domain," *IEEE Trans. Power Electron.*, vol. 33, no. 5, pp. 4015–4022, May 2018.

[18] S. Wang, Z. Liu, J. Liu, D. Boroyevich, and R. Burgos, "Small-signal modeling and stability prediction of parallel droop-controlled inverters based on terminal characteristics of individual inverters," *IEEE Trans. Power Electron.*, vol. 35, no. 1, pp. 1045–1063, Jan. 2020.

[19] A. Rygg, M. Molinas, C. Zhang, and X. Cai, "A modified sequence-domain impedance definition and its equivalence to the dq-domain impedance definition for the stability analysis of AC power electronic systems," *IEEE J. Emerg. Sel. Topics Power Electron.*, vol. 4, no. 4, pp. 1383–1396, 2016.

[20] M. Schweizer and J. W. Kolar, "Shifting input filter resonances—An intelligent converter behavior for maintaining system stability," in *Proc. Int. Power Electron. Conf. ECCE Asia*, May 2010, pp. 906–913.

[21] L. Harnefors, M. Bongiorno, and S. Lundberg, "Input-admittance calculation and shaping for controlled voltage-source converters," *IEEE Trans. Ind. Electron.*, vol. 54, no. 6, pp. 3323–3334, Dec. 2007.

[22] B. Wen, D. Boroyevich, R. Burgos, P. Mattavelli, and Z. Shen, "Analysis of D-Q small-signal impedance of grid-tied inverters," *IEEE Trans. Power Electron.*, vol. 31, no. 1, pp. 675–687, Jan. 2016.

[23] L. Yang, Y. Chen, and A. Luo, "Effect of phase-locked loop on small-signal perturbation modelling and stability analysis for three-phase LCL-type inverter connected to weak grid," *IET Renewable Power Gener.*, vol. 13, no. 1, pp. 86–93, 2019.

[24] Z. Shuai, Y. Li, W. Wu, C. Tu, A. Luo, and Z. J. Shen, "Divided DQ small-signal model: A new perspective for the stability analysis of three-phase grid-tied inverters," *IEEE Trans. Ind. Electron.*, vol. 66, no. 8, pp. 6493–6504, Aug. 2019.
[25] T. Messo, J. Jokipii, A. Mäkinen, and T. Suntio, "Modeling the grid synchronization induced negative-resistor-like behavior in the output impedance of a three-phase photovoltaic inverter," in *Proc. 4th IEEE Int. Symp. Power Electron. Distrib. Gener. Syst.*, 2013, pp. 1–7.
[26] B. Wen, R. Burgos, D. Boroyevich, P. Mattavelli, and Z. Shen, "AC stability analysis and dq frame impedance specifications in power-electronics-based distributed power systems," *IEEE J. Emerg. Sel. Topics Power Electron.*, vol. 5, no. 4, pp. 1455–1465, Dec. 2017.
[27] W. Wang, Z. Zeng, Z. Wei, and H. Xiao, "A simplified D-Q small-signal modelling method of rid-tied inverters for stability analysis," in *Proc. 9th IPEMC-ECCE Asia*, Nangjing, China, Nov./Dec. 2020, pp. 2893–2899.
[28] J. Xu, S. Xie, Q. Qian, and B. Zhang, "Adaptive feedforward algorithm without grid impedance estimation for inverters to suppress grid current instabilities and harmonics due to grid impedance and grid voltage distortion," *IEEE Trans. Ind. Electron.*, vol. 64, no. 9, pp. 7574–7586, Sep. 2017.
[29] H. Gong, D. Yang, and X. Wang, "Impact analysis and mitigation of synchronization dynamics for DQ impedance measurement," *IEEE Trans. Power Electron.*, vol. 34, no. 9, pp. 8797–8807, Sep. 2019.

Zhijie Zeng was born in Fujian Province, China. He received the B.S. degree in 2018 from Northeastern University, Shenyang, China, and the M.S. degree in 2021 from Southeast University, Nanjing, China.

He is currently an Engineer with Fujian Electric Power Research Institute, State Grid Corporation of China (SGCC), Fuzhou, China. His research interests include modeling and stability of new energy generation systems.

Huafeng Xiao (Senior Member, IEEE) was born in Hubei Province, China. He received the B.S., M. S., and Ph.D. degrees in electrical engineering from the Nanjing University of Aeronautics and Astronautics (NUAA), Nanjing, China, in 2004, 2007, and 2010, respectively.

He joined the Faculty of power electronics in 2011, and is currently a Professor with the College of Electrical Engineering, Southeast University (SEU), Nanjing, China. From 2015 to 2016, he was a Postdoctoral Fellow with the Department of Electrical and Computer Engineering, Ryerson University, Toronto, ON, Canada. From August 2016 to 2017, he was a Postdoctoral Fellow with the Department of Electrical and Computer Engineering, McGill University, Montreal, QC, Canada. He has authored more than 100 technical papers in journals and conference proceedings, and held 36 China patents and 1 U.S. patent, and authored two books as well. His research interests include transformerless photovoltaic power systems, and high frequency soft-switching conversions.

Chenhui Niu was born in Lioaning Province, China. He received the B.S. degree in 2006 from North China Electric Power Universty, Beijing, China, and the M.S. degree in 2010 from The University of New South Wales, Sydney, NSW, Australia.

He is currently the Director of Science and Technology Center, China Huaneng Jiangsu Company, Nanjing, China. His research interests include test and verification of new energy generation systems.

Jie Chen (Member, IEEE) received the B.S. and Ph.D. degrees in electrical engineering from the Nanjing University of Aeronautics and Astronautics (NUAA), Nanjing, China, in 2004 and 2011, respectively.

In October 2011, he joined the College of Automation Engineering, NUAA, as a Lecturer, where he is currently an Associate Professor. From November 2018 to November 2019, he was a Visiting Faculty with the Center for Ultra-Wide-Area Resilient Electric Energy Transmission Networks (CURENT), Department of Electrical Engineering and Computer Science, The University of Tennessee, Knoxville, TN, USA. His research interests include modeling, design and control of power electronic converters or systems, renewable energy generation systems, and power system of more electric aircraft.

Ziyi Wang was born in Jiangsu Province, China. He received the B.S. degree in 2018 from the Nanjing Institute of Technology, Nanjing, China, and the M.S. degree in 2021 from Southeast University, Nanjing, China.

He is currently an Engineer with Shanghai Electric Power Corporation, State Grid Corporation of China (SGCC), Shanghai, China. His research interests include modeling and fault analysis of UHVdc systems.

Xu Wu was born in Jiangsu Province, China. He received the B.S. degree from Jiangsu University, Zhenjiang, China, in 2020. He is currently working toward the Ph.D. degree with the Department of Electrical Engineering, Southeast University, Nanjing, China.

His research interests include modeling and stability of new energy generation systems.

Ming Cheng (Fellow, IEEE) received the B.Sc. and M.Sc. degrees from the Department of Electrical Engineering, Southeast University, Nanjing, China, in 1982 and 1987, respectively, and the Ph.D. degree from the Department of Electrical and Electronic Engineering, The University of Hong Kong, Hong Kong, in 2001, all in electrical engineering.

Since 1987, he has been with Southeast University, where he is currently a Chair Professor with the School of Electrical Engineering and the Director of the Research Center for Wind Power Generation. From January 2011 to April 2011, he was a Visiting Professor with Wisconsin Electric Machine and Power Electronics Consortium, University of Wisconsin, Madison, WI, USA. He has authored or coauthored more than 360 technical papers and 4 books and is the holder of 100 patents in these areas. His teaching and research interests include electrical machines, motor drives for electric vehicles, and renewable energy generation.

Prof. Cheng is a Fellow of the Institution of Engineering and Technology. He has served as the chair and organizing committee member for many international conferences. He is a Distinguished Lecturer of the IEEE Industry Applications Society (IAS) in 2015/2016.